

Effects of jet pattern on single-phase cooling performance of hybrid micro-channel/micro-circular-jet-impingement thermal management scheme

Myung Ki Sung, Issam Mudawar *

Boiling and Two-Phase Flow Laboratory (BTPFL), Purdue University International Electronic Cooling Alliance (PIECA), Mechanical Engineering Building, 585 Purdue Mall West Lafayette, IN 47907-2088, USA

Received 19 December 2007; received in revised form 1 February 2008
Available online 28 April 2008

Abstract

This study explores the single-phase cooling performance of a hybrid cooling module in which a series of micro-jets deposit coolant into each channel of a micro-channel heat sink. This creates symmetrical flow in each micro-channel, and the coolant is expelled through both ends of the micro-channel. Three micro-jet patterns are examined, decreasing-jet-size (relative to center of channel), equal-jet-size and increasing-jet-size. The performance of each pattern is examined experimentally and numerically using HFE 7100 as working fluid. Indirect refrigeration cooling is used to reduce the coolant's temperature in order to produce low wall temperatures during high-flux heat dissipation. A single heat transfer coefficient correlation is found equally effective at correlating experimental data for all three jet patterns. Three-dimensional numerical simulation using the standard $k-\epsilon$ model shows excellent accuracy in predicting wall temperatures. Numerical results show the hybrid cooling module involves complex interactions of impinging jets and micro-channel flow. Increasing the coolant's flow rate strengthens the contribution of jet impingement to the overall cooling performance, and decreases wall temperature. However, this advantage is realized at the expense of greater wall temperature gradients. The decreasing-jet-size pattern yields the highest convective heat transfer coefficients and lowest wall temperatures, while the equal-jet-size pattern provides the greatest uniformity in wall temperature. The increasing-jet-size pattern produces complex flow patterns and greater wall temperature gradients, which are caused by blockage of spent fluid flow due to the impingement from larger jets near the channel outlets.

© 2008 Elsevier Ltd. All rights reserved.

1. Introduction

1.1. Micro-channel and jet-impingement cooling

Micro-channel flow and jet-impingement are undoubtedly two of the most powerful thermal solutions for situations demanding high-flux heat removal. This includes high-performance computer chips, hybrid-vehicle power electronics, military avionics, radars, and defense laser and microwave directed-energy weapon systems [1].

Micro-channel heat sinks have been studied extensively for electronics cooling. In an often-cited study, Tuckerman

and Pease [2] were able to dissipate up to 790 W/cm^2 using a water-cooled micro-channel heat sink. They pointed out two key problems of micro-channel heat sinks, high pressure drop and large temperature gradients along the flow direction. Bowers and Mudawar [3] achieved single-phase cooling heat fluxes as high as 3000 W/cm^2 in micro-tubes using water as working fluid. Both numerical and analytical methods have been used to model single-phase fluid flow and heat transfer in micro-channel heat sinks [4–6]. Qu and Mudawar [4] showed the pressure drop and heat transfer characteristics of micro-channel heat sinks could be accurately predicted by solving the conventional Navier–Stokes' and energy equations.

Single-phase jet-impingement cooling has also been investigated both experimentally [7–9] and numerically

* Corresponding author. Tel.: +1 765 494 5705; fax: +1 765 494 0539.
E-mail address: mudawar@ecn.purdue.edu (I. Mudawar).

Nomenclature

A_t	top test surface area of copper heating block ($1.0 \times 2.0 \text{ cm}^2$)	q''_{eff}	effective heat flux based on top test surface area of copper block, P_w/A_t
C_1, C_2, C_3	empirical constants	r	radius measured from jet centerline
D_{jet}	Diameter of micro-jet	r_b	radial location where boundary layer reaches film thickness
H	height of unit cell	r_c	critical radius corresponding to onset of turbulent zone
H_{ch}	height of micro-channel	Re	Reynolds number
H_{jet}	height (length) of micro-jet	Re_{jet}	jet Reynolds number, $U_{\text{jet}}D_{\text{jet}}/\nu_f$
H_{th}	height from thermocouple hole to unit cell bottom boundary	$Re_{\text{jet},m}$	jet Reynolds number based on mean velocity of all jets in a given jet pattern
H_w	height from unit cell bottom boundary to bottom wall of micro-channel	r_j	radius of circular jet
h	height of wall jet; convective heat transfer coefficient, $q''_{\text{eff}}/(T_s - T_{\text{in}})$	r_s	radial extent of stagnation zone
\bar{h}_{ch1}	mean convective heat transfer coefficient for micro-channel region 1	T	Temperature
\bar{h}_{ch2}	mean convective heat transfer coefficient for micro-channel region 2	T_{in}	fluid temperature at test module inlet
\bar{h}_{jet}	mean convective heat transfer coefficient for jet-impingement region	T_{out}	fluid temperature at test module outlet
\bar{h}_L	mean convective heat transfer coefficient inside micro-channel	T_{tci}	temperature measure by thermocouple i ($i = 1-4$)
k	thermal conductivity	U_{jet}	mean jet velocity
l	parameter used in determining laminar layer thickness	W	width of unit cell
L	length of unit cell (also length of micro-channel)	W_{ch}	width of micro-channel
$L_{\text{jet},i}$	length of micro-channel associated with jet i	W_w	half-width of copper wall separating micro-channels
L_{jet}	pitch of micro-jet	x	Cartesian coordinate
L_1, L_2, L_3, L_4	distance between thermocouple holes	y	Cartesian coordinate
\dot{m}	mass flow rate of entire cooling module	z	Cartesian coordinate
N_i	number of jets of size i in single micro-channel	<i>Greek symbols</i>	
N_{jet}	total number of jets in single micro-channel	δ	hydrodynamic boundary layer thickness
Nu	Nusselt number	δ_{th}	thermal boundary layer thickness
\overline{Nu}_L	average Nusselt number	ν	kinematic viscosity
p_h	perimeter of micro-channel, $2(W_{\text{ch}} + H_{\text{ch}})$	ρ	density
P	Pressure	<i>Subscripts</i>	
P_{in}	fluid pressure at test module inlet	ch	channel
P_{out}	fluid pressure at test module outlet	f	liquid
Pr	Prandtl number	in	test module inlet
P_w	total electrical power input to cartridge heaters	out	test module outlet
		tci	thermocouple i ($i = 1-4$).

[10–12]. Wadsworth and Mudawar [9] conducted confined slot jet experiments using FC-72 as working fluid and developed a superpositioning scheme for correlating single-phase heat transfer coefficient data. Baydar and Ozmen [12] demonstrated that the $k-\epsilon$ model accurately predicts the flow characteristics of confined air jets.

Overall, micro-channel heat sinks offer several important attributes, including the ability to dissipate very large heat fluxes from small surface areas, compactness and small coolant inventory. A key drawback of single-phase micro-channel heat sinks is the coolant temperature rise along the micro-channel can cause appreciable temperature gradients in the heat-dissipating device to which the heat

sink is attached. Another drawback is large pressure drop. Jet-impingement cooling has the capacity to dissipate very large heat fluxes corresponding to relatively small pressure drop. However, jets concentrate most of the cooling within the immediate vicinity of the stagnation zone. Multiple jets are commonly used to diffuse this effect by creating several high-flux impingement regions that are distributed along the surface of the heat-dissipating device.

1.2. Merits of low temperature refrigeration

Regardless which cooling scheme is used, dissipating very large heat fluxes can lead to unacceptably high device

temperatures. All electronic devices have upper temperature limits that are dictated by material and performance constraints. One effective means for maintaining the device temperature below this limit during high-flux heat dissipation is to greatly decrease the coolant temperature. One example of a successful low temperature cooling system is the Kleemenko cooler, which provides 80 W of refrigeration for device cooling at $-96\text{ }^{\circ}\text{C}$ [13]. Aside from thermal benefits, low temperatures provide significant enhancement in device functionality and reliability. Naeemi and Meindl [14] demonstrated 4.3 times higher CMOS chip performance at $-100\text{ }^{\circ}\text{C}$ than at $85\text{ }^{\circ}\text{C}$. Schmidt and Notohardjono [15] showed low temperature cooling offers orders of magnitude improvement in reliability. Overall, low temperatures facilitate faster switching times of semiconductor devices, increase circuit speed (due to lower electrical resistance of interconnecting materials), reduce thermally induced failures, and improve device performance by decreasing current leakage.

Refrigeration cooling can be implemented in one of two configurations, direct-refrigeration cooling and indirect-refrigeration cooling. Direct refrigeration involves inserting the cooling module as an evaporator in a vapor compression cycle, and using the refrigerant as coolant for the electronic device. Indirect-refrigeration cooling involves using a separate cooling loop in which a liquid coolant is used to remove the dissipated heat, which is rejected a separate vapor compression cycle. While the direct-refrigeration system is simpler and more compact, the indirect-refrigeration system provides greater flexibility in coolant selection, as well as allows the use of a non-pressurized cooling module.

1.3. Objectives of study

Recently, the authors of the present study proposed a hybrid cooling scheme that combines the cooling benefits of micro-channel flow and micro-circular-jet-impingement [16,17]. With this hybrid cooling scheme, the coolant is introduced gradually as a series of jets into each micro-channel of a micro-channel heat sink, and is expelled symmetrically through both ends of the micro-channel. Unlike conventional micro-channels, where the temperatures of both the coolant and the device to which the micro-channel heat sink is attached increase along the direction of fluid flow, the hybrid scheme supplies low temperature coolant at various locations along the micro-channel. This helps to enhance temperature uniformity of both coolant and device. Another benefit of the hybrid scheme is a reduction in pressure drop compared to conventional micro-channel heat sinks. The hybrid cooling scheme is also superior to multi-jet-impingement modules in its ability to better manage the flow of spent coolant, prevent flow instabilities, and reduce flow blockage. The earlier authors' studies involved equally-sized micro-circular-jets that are equally spaced along the micro-channel.

The present study is an extension of the authors' earlier work and aims to explore the benefits of utilizing differently sized jets along the micro-channel. Three different jet patterns are compared. The first, decreasing-jet-size pattern, consists of jets that decrease in size symmetrically from the center of the micro-channel towards the two ends. The second, equal-jet-size pattern, consists of jets of equal size uniformly distributed along the micro-channel, like those used in the authors' earlier studies. The third, increasing-jet-size pattern, consists of jets that increase in size from the center of the micro-channel towards the two ends. The same total flow area of all jets is used for each jet pattern. The key objective in examining these three configurations is to explore any potential cooling benefits that may be realized as a result of modulating the relative contributions of jet impingement and micro-channel flow in various regions of the micro-channel. To further enhance cooling performance, the three jet patterns are tested in an indirect-refrigeration cooling system. Two ultimate cooling objectives are to achieve, for a given flow rate, the highest possible heat transfer coefficient (i.e., lowest wall temperature) and lowest wall temperature gradients. Numerical simulation is used to predict both the complex micro-jet/micro-jet flow interactions and wall temperature distribution. Also presented is a simple, yet very effective scheme for correlating single-phase heat transfer coefficient data.

2. Experimental methods

2.1. Test module

The layered construction and assembly of the test module are illustrated in Fig. 2. The test module consists of a copper heating block, a micro-jet plate, an upper housing, a bottom housing, lower support plates, and 16 cartridge heaters. Liquid HFE 7100 is supplied from the upper housing into a plenum in the upper housing above the micro-jet plate. The coolant flows through holes in the micro-jet plate in the form of jets that impinge inside the micro-channels. The flow splits into two equal and opposite parts in the micro-channels, each is expelled into one of two plenums in the bottom housing. The micro-channels are formed by cutting five 1.0-mm wide and 3-mm deep slots equidistantly within the 1.0-cm width of the top $1.0 \times 2.0\text{ cm}^2$ test surface area of the copper block. The copper block is tapered in two steps to help ensure uniform temperature along the top surface. The heights of these steps are based on numerical three-dimensional simulation of the test module. Heat is supplied to the micro-channels from the 16 cartridge heaters that are inserted into the underside of the copper block. The total electrical power input to the cartridge heaters is measured by a Yokogawa WT 210 wattmeter. Both the upper and bottom housings are machined from high-temperature G-11 fiberglass plastic. Four stainless steel pins are inserted between the

micro-jet plate and the bottom housing to accurately align the jets relative to the micro-channels. The copper heating block is wrapped in multiple layers of ceramic fiber, and mounted atop a solid ceramic plate to help minimize heat loss. Four type-T thermocouples are inserted below the micro-channel bottom wall to monitor stream-wise temperature distribution. An absolute pressure transducer and a type-T thermocouple are connected to the inlet plenum of the test module. Another absolute pressure transducer and a second thermocouple are each connected to one of the outlet plenums.

2.2. Jet patterns

Three different micro-jet patterns are examined; each pattern is formed in a separate micro-jet plate. In the first micro-jet plate, jets decrease in size along each side of the micro-channel. The second plate has equally-sized jets, and, in the third plate, jets increase in size along each side of the micro-channel. In each plate, five parallel arrays of circular holes are drilled within the 1-cm width facing the five micro-channels. It is important to emphasize that the sum of flow areas of all jets is the same for all three micro-jet plates. The micro-jet plates are fabricated from oxygen-free copper.

2.3. Flow loop

Fig. 1 shows a schematic diagram of the cooling system that is configured to deliver low temperature HFE 7100 liquid at the desired pressure and flow rate to the test module. Heat is rejected from the HFE 7100 liquid to a

secondary refrigeration system via a heat exchanger. The refrigeration system uses feedback control to regulate the temperature of the HFE 7100 liquid at the heat exchanger outlet to within $\pm 0.5^\circ\text{C}$. The coolant flow rate and pressure are controlled by two needle valves situated upstream and downstream of the test module, as well as a bypass valve. The coolant flow rate is measured by a Coriolis flow meter.

Electric power is supplied to the test module and increased in small increments after the desired test module inlet conditions are reached. Once steady-state is reached following each power increment, the module inlet pressure, P_{in} , outlet pressure, P_{out} , inlet temperature, T_{in} , outlet temperature, T_{out} , heating block temperatures, T_{tc1} – T_{tc4} , and electrical power input, P_W , are all recorded for later processing. Measurement uncertainties associated with the pressure transducers, flow meter, wattmeter, and thermocouples are 0.5%, 0.1%, 0.5%, and 0.3°C , respectively. A numerical 3-D model of the entire test module yielded a worst-case heat loss (corresponding to the lowest coolant flow rate tested) of less than 8% of the electrical power input. The heat fluxes reported in the present paper are therefore based on the measured electrical power input. The experimental operating conditions of this study are listed in Table 1.

Table 1
Experimental operating conditions

Working fluid	Inlet temperature T_{in} ($^\circ\text{C}$)	Inlet flow rate \dot{m} (g/s)	Effective heat flux q''_{eff} (W/cm^2)
HFE 7100	-40 to 20	11.1–55.9	16.1–304.9

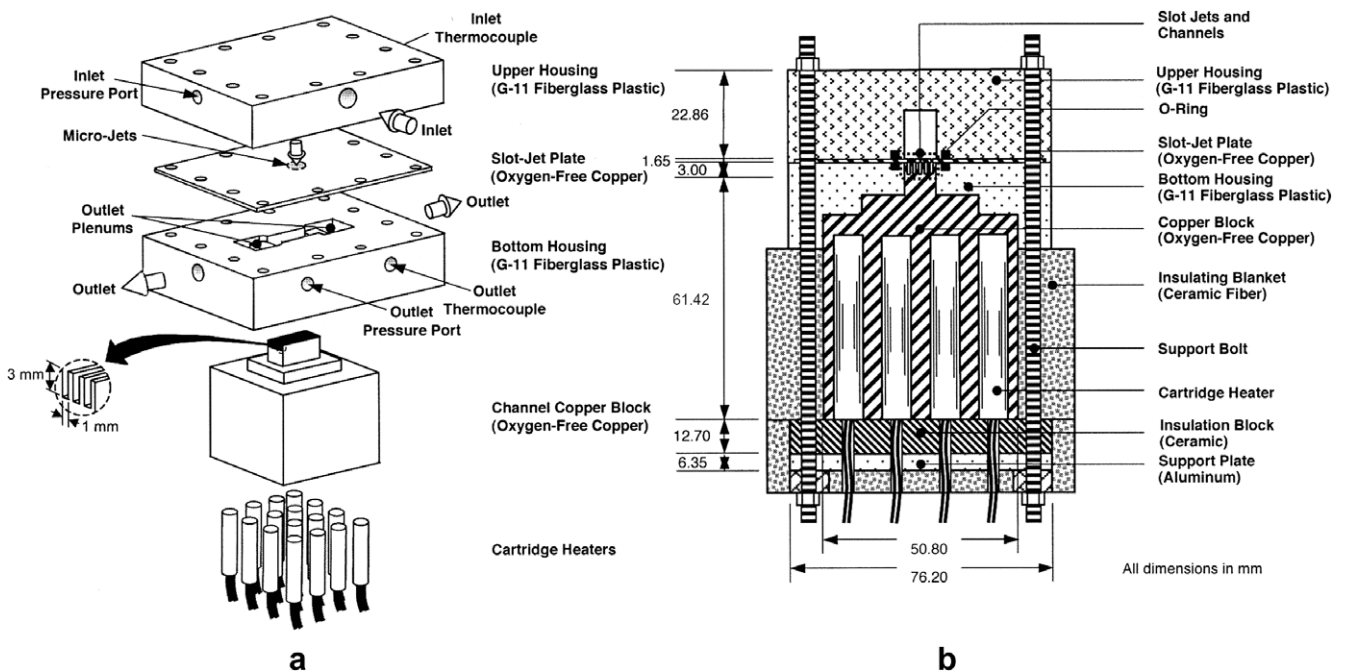


Fig. 1. (a) Test module construction. (b) Cross-section of module assembly.

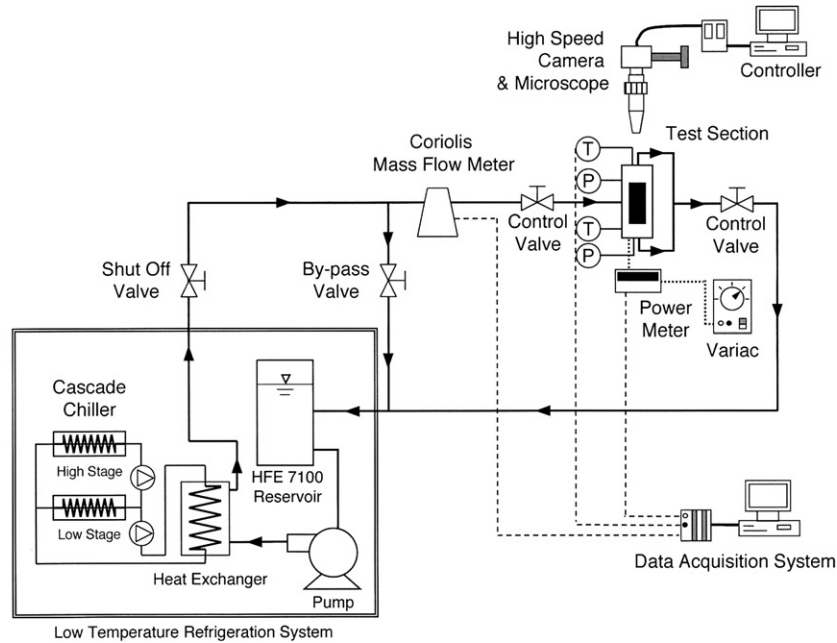


Fig. 2. Schematic of flow control system.

3. Numerical scheme

Fig. 3a shows a unit cell consisting of a single micro-channel, portion of the micro-jet plate facing the same micro-channel, and surrounding solid. This figure shows the different geometrical parameters of the unit cell as well as locations of the thermocouples in the copper block. Due to symmetry, a computational domain consisting of only one quarter of the unit cell is required. Fig. 3b shows the detail geometrical parameters of the three micro-jet plates. Table 2 provides all dimensions of the unit cell and the jet plates.

FLUENT 6.2.16 [18] is used to compute flow fields and heat transfer characteristics of the hybrid cooling module. The computational mesh is constructed using Gambit 2.2.30 [19]. The model used here assumes steady, turbulent and incompressible flow with constant properties. The standard two-equation $k-\epsilon$ turbulent model [20] is used for closure of the Reynolds stress tensor. The governing conservation equations as well as boundary conditions and the effects of mesh size are detailed in two previous studies by the authors [16,17].

3.1. Determination of extent of laminar zone

Fig. 4 shows the flow field along a heated surface for a circular free jet. To determine the radial distance of the turbulent zone from the jet centerline, laminar flow is imposed on the computational domain from the jet inlet to the stagnation zone, and a portion of the wall jet surrounding the stagnation zone. The procedure for determining the upstream radial location of the turbulent zone and laminar thickness is described in [17]. Key equations for wall layer

thickness and radial locations of the individual zones are as follows:

$$h = \frac{D_{\text{jet}}^2}{8r} \quad \text{for } 0 < r < r_s, \quad (1a)$$

$$h = \left(\frac{D_{\text{jet}}^2}{8r} \right) + \left\{ 1 - \frac{2\pi}{3\sqrt{3}c^2} \right\} \delta \quad \text{for } r_s < r < r_b, \quad (1b)$$

$$h = \frac{8\pi}{3\sqrt{3}} \frac{(r^3 + l^3)}{D_{\text{jet}} Re_{\text{jet}} r} \quad \text{for } r_b < r < r_c, \quad (1c)$$

where

$$\delta^2 = \frac{(1.402)^3 \sqrt{3}}{\pi - 1.402\sqrt{3}} \frac{r}{D_{\text{jet}} Re_{\text{jet}}}, \quad (2a)$$

$$l = 0.3296 D_{\text{jet}} Re_{\text{jet}}^{1/3}, \quad (2b)$$

and

$$r_b = 0.1834 D_{\text{jet}} Re_{\text{jet}}^{1/3}. \quad (2c)$$

The computational domain in FLUENT is therefore divided into two sub-zones, a laminar zone and a turbulent zone. For each jet pattern, the laminar thickness for each jet-size is determined and the smallest laminar zone height is used for all jets. Laminar flow is imposed on the flow domain between the jet inlet and the stagnation zone, as well as up to height $h(r)$ from the well. Turbulence is permitted everywhere else in the computational domain.

3.2. Determination of jet velocities

Jet velocities of differently sized jets can be related to one another by equating their pressure drop. Consider a cool-

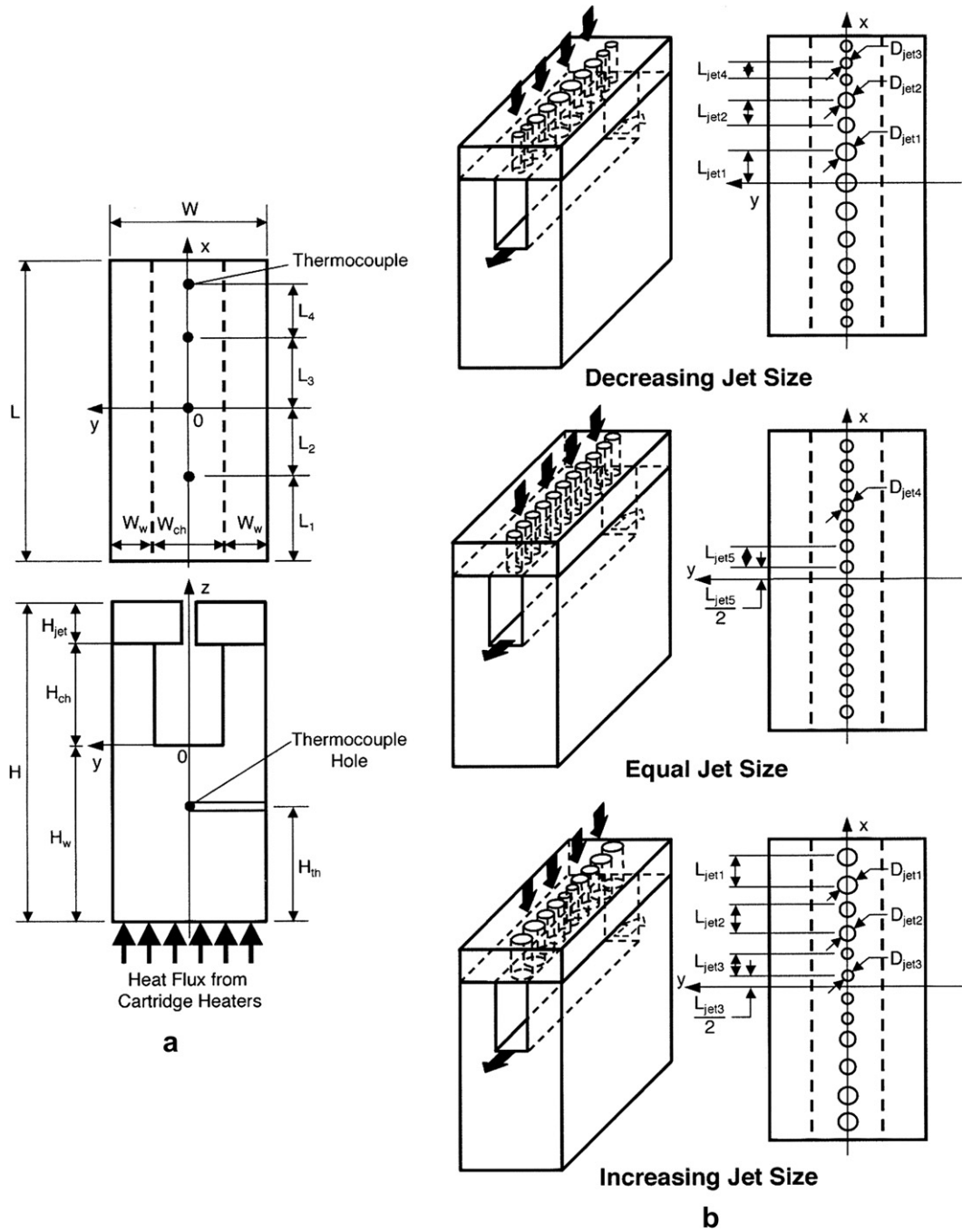


Fig. 3. Schematic of unit cell illustrating (a) overall dimensions and thermocouple locations and (b) jet patterns.

ing module that contains three different jet sizes, D_{jet1} , D_{jet2} and D_{jet3} . Equal pressure drop requires that

$$\begin{aligned} \Delta P_1 = \Delta P_2 = \Delta P_3 &= f \frac{H_{jet}}{D_{jet1}} \frac{\rho_f U_{jet1}^2}{2} \\ &= f \frac{H_{jet}}{D_{jet2}} \frac{\rho_f U_{jet2}^2}{2} = f \frac{H_{jet}}{D_{jet3}} \frac{\rho_f U_{jet3}^2}{2}, \end{aligned} \quad (3)$$

where the pressure drop coefficient, f , is inversely proportional to jet Reynolds [21]

$$f = K Re_{jet}^{-1}, \quad (4)$$

and K is fairly constant for the conditions of the present study. Eqs. (3) and (4) allow the jet velocities to be related to one another.

$$U_{jet2} = \frac{D_{jet2}^2}{D_{jet1}^2} U_{jet1} \quad (5a)$$

and

$$U_{jet3} = \frac{D_{jet3}^2}{D_{jet1}^2} U_{jet1}. \quad (5b)$$

Table 2
Dimensions of unit cell

L (mm)	L_1 (mm)	L_2 (mm)	L_3 (mm)	L_4 (mm)	W (mm)	W_w (mm)	H (mm)	H_{jet} (mm)	H_{ch} (mm)	H_w (mm)	H_{th} (mm)	D_{jet1} (mm)	D_{jet2} (mm)	D_{jet3} (mm)	D_{jet4} (mm)	D_{jet5} (mm)	L_{jet1} (mm)	L_{jet2} (mm)	L_{jet3} (mm)	L_{jet4} (mm)	L_{jet5} (mm)
20.00	4.00	6.00	3.00	6.00	1.83	1.00	14.27	1.65	3.00	7.62	5.08	0.60	0.45	0.30	0.42	0.42	1.84	1.62	1.44	1.23	1.43

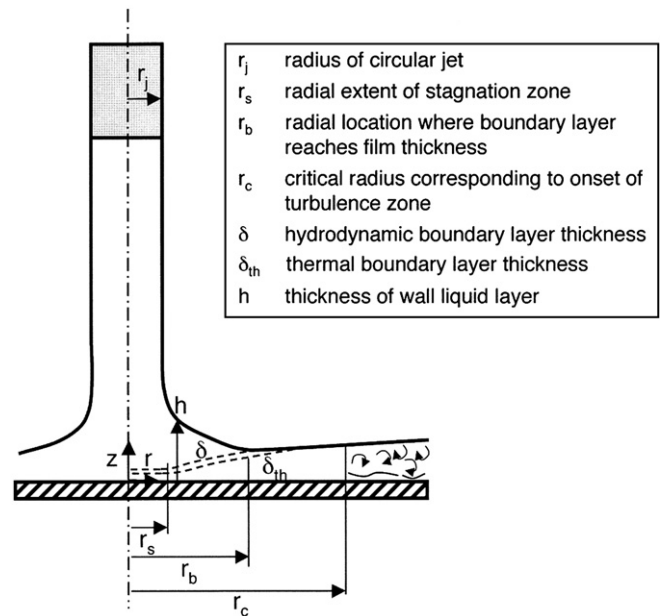


Fig. 4. Fluid flow regimes for free circular impinging jet with $Pr_f > 1$.

Then U_{jet1} can be determined from continuity.

$$\begin{aligned} \dot{m}_{total} = & N_1 \rho_f \left(\frac{\pi D_{jet1}^2}{4} \right) U_{jet1} \\ & + N_2 \rho_f \left(\frac{\pi D_{jet2}^2}{4} \right) \left(\frac{D_{jet2}^2}{D_{jet1}^2} U_{jet1} \right) \\ & + N_3 \rho_f \left(\frac{\pi D_{jet3}^2}{4} \right) \left(\frac{D_{jet3}^2}{D_{jet1}^2} U_{jet1} \right), \end{aligned} \quad (6)$$

where N_i is the total number jets of diameter D_{jeti} . The velocities of the other jets can be determined using Eqs. (5a) and (5b).

4. Correlation of heat transfer data

A superpositioning technique is used to correlate the single-phase heat transfer data for the three jet patterns. This technique seeks to assign dominant heat transfer mechanisms to different portions of the heat transfer area. This technique, which was originally developed by Wadsworth and Mudawar [9] for confined slot jets, was very effective at correlating the present authors' single-phase data for a hybrid micro-channel/micro-jet-impingement module with equal-jet-size [16].

The superpositioning technique consists of applying different correlations of the general form

$$\frac{\overline{Nu}}{Pr_f^{0.4}} = f(Re) \quad (7)$$

to the different surface regions. Fig. 5 illustrates the different regions associated with a single jet. The surface consists of an impingement region, two identical bottom wall

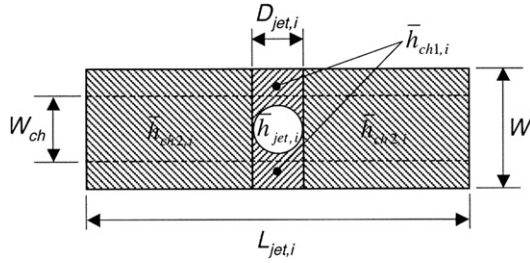


Fig. 5. Schematic of superpositioning technique for correlating single-phase heat transfer data.

regions, and a micro-channel flow region. Assuming surface temperature is uniform across the entire wetted surface, the superpositioning technique yields the following relation for overall heat transfer coefficient, \bar{h}_L :

$$\bar{h}_L p_h L = \sum_{i=1}^{N_{\text{jet}}} \left\{ \bar{h}_{\text{jet},i} \left[\frac{\pi D_{\text{jet},i}^2}{4} \right] + \bar{h}_{\text{ch1},i} \left[\left(W_{\text{ch}} D_{\text{jet},i} - \frac{\pi D_{\text{jet},i}^2}{4} \right) \right] + \bar{h}_{\text{ch2},i} \left[p_h L_{\text{jet},i} - \left(W_{\text{ch}} D_{\text{jet},i} + \frac{\pi D_{\text{jet},i}^2}{4} \right) \right] \right\}, \quad (8)$$

where N_{jet} is the number of micro-jets for a single micro-channel and p_h the micro-channel perimeter. Since channel velocity increases away from the central jets towards the outlet due to the increasing flow rate, Eq. (8) is written to allow for variations in the values of heat transfer coefficients between successive jet cells similar to those depicted in Fig. 5. Eq. (8) assumes jets are symmetrically situated around the center of the micro-channel. As shown in Fig. 3, this is the case for both the equal-jet-size and increasing-jet-size patterns examined in this study. However, the decreasing-jet-size pattern includes a jet at the center of the micro-channel, which does not conform to Eq. (8). Following is a correlation technique for symmetrical jet patterns that do not include a central jet. Variations in the correlation for patterns including a central jet will be discussed afterwards.

Eq. (8) can be represented in the dimensionless form

$$\overline{Nu}_L = \frac{\bar{h}_L L}{k_f} = \sum_{i=1}^{N_{\text{jet}}} \left\{ \left[\frac{\bar{h}_{\text{jet},i} \left(\frac{\pi D_{\text{jet},i}^2}{4 p_h} \right)}{k_f} \right] + \left[\frac{\bar{h}_{\text{ch1},i} \left(\frac{W_{\text{ch}} D_{\text{jet},i} - \frac{\pi D_{\text{jet},i}^2}{4}}{p_h} \right)}{k_f} \right] + \left[\frac{\bar{h}_{\text{ch2},i} \left[L_{\text{jet},i} - \frac{W_{\text{ch}} D_{\text{jet},i}}{p_h} \left(1 + \frac{\pi D_{\text{jet},i}^2}{4 W_{\text{ch}} D_{\text{jet},i}} \right) \right]}{k_f} \right] \right\}. \quad (9)$$

The Reynolds numbers used to characterize heat transfer in the different surface regions depicted in Fig. 5 are defined as

$$Re_{\text{jet},i} = \frac{U_{\text{jet},i} D_{\text{jet},i}}{v_f}, \quad (10a)$$

$$Re_{\text{ch1},i} = \frac{U_{\text{ch1},i} \left(\frac{W_{\text{ch}} D_{\text{jet},i} - \frac{\pi D_{\text{jet},i}^2}{4}}{p_h} \right)}{v_f}, \quad (10b)$$

and

$$Re_{\text{ch2},i} = \frac{U_{\text{ch2},i} \left[L_{\text{jet},i} - \frac{W_{\text{ch}} D_{\text{jet},i}}{p_h} \left(1 + \frac{\pi D_{\text{jet},i}^2}{4 W_{\text{ch}} D_{\text{jet},i}} \right) \right]}{v_f}. \quad (10c)$$

Due to the Bernoulli effect, the sidewall characteristic velocity is assumed equal to the jet velocity. The channel velocity can be determined from mass conservation, accounting for the gradual increase in flow rate away from the center of the micro-channel.

$$U_{\text{ch},i} = U_{\text{jet},i} \quad (11a)$$

and

$$U_{\text{ch2},i} = \sum_{j=1}^i \frac{U_{\text{jet},j} \frac{\pi D_{\text{jet},j}^2}{4}}{W_{\text{ch}} H_{\text{ch}}}. \quad (11b)$$

Therefore, the heat transfer correlation can be written as

$$\begin{aligned} \frac{\overline{Nu}_L}{\text{Pr}_f^{0.4}} &= \sum_{i=1}^{N_{\text{jet}}} \left\{ C_1 Re_{\text{jet},i}^a \left(\frac{D_{\text{jet},i}}{p_h} \right) + C_2 Re_{\text{ch1},i}^b + C_3 Re_{\text{ch2},i}^c \right\} \\ &= \sum_{i=1}^{N_{\text{jet}}} \left\{ C_1 Re_{\text{jet},i}^a \left(\frac{D_{\text{jet},i}}{p_h} \right) + C_2 Re_{\text{jet},i}^b \left(\frac{W_{\text{ch}} D_{\text{jet},i} - \frac{\pi D_{\text{jet},i}^2}{4}}{p_h D_{\text{jet},i}} \right) \right. \\ &\quad \left. + C_3 Re_{\text{jet},i}^c \left[\sum_{j=1}^i \left\{ \frac{\left(\frac{U_{\text{jet},j}}{U_{\text{jet},i}} \right) \frac{\pi D_{\text{jet},j}^2}{4}}{W_{\text{ch}} H_{\text{ch}}} \right\} \right] \right. \\ &\quad \left. \times \left[\frac{L_{\text{jet},i}}{D_{\text{jet},i}} - \frac{W_{\text{ch}}}{p_h} \left(1 + \frac{\pi D_{\text{jet},i}^2}{4 W_{\text{ch}} D_{\text{jet},i}} \right) \right] \right\}. \quad (12) \end{aligned}$$

Eq. (12) can also be written as

$$\begin{aligned} \frac{\overline{Nu}_L}{\text{Pr}_f^{0.4}} &= \sum_{i=1}^{N_{\text{jet}}} \sum_{j=1}^i \left\{ C_1 Re_{\text{jet},i}^a \left(\frac{D_{\text{jet},i}}{p_h} \right) \left(\frac{1}{i} \right) \right. \\ &\quad \left. + C_2 Re_{\text{jet},i}^b \left(\frac{W_{\text{ch}} D_{\text{jet},i} - \frac{\pi D_{\text{jet},i}^2}{4}}{p_h D_{\text{jet},i}} \right) \left(\frac{1}{i} \right) \right. \\ &\quad \left. + C_3 Re_{\text{jet},i}^c \left[\frac{\left(\frac{U_{\text{jet},j}}{U_{\text{jet},i}} \right) \frac{\pi D_{\text{jet},j}^2}{4}}{W_{\text{ch}} H_{\text{ch}}} \left[\frac{L_{\text{jet},i}}{D_{\text{jet},i}} - \frac{W_{\text{ch}}}{p_h} \right] \right. \right. \\ &\quad \left. \left. \times \left(1 + \frac{\pi D_{\text{jet},i}^2}{4 W_{\text{ch}} D_{\text{jet},i}} \right) \right] \right\}. \quad (13) \end{aligned}$$

As indicated earlier, Eqs. (12) and (13) are valid for jet patterns that do not include a central jet. For patterns with a

central jet, these equations must be modified by including the following term for each side of the micro-channel.

$$C_1 Re_{jet,1}^a \left(\frac{D_{jet,1}/2}{p_h} \right) + C_2 Re_{jet,1}^b \left(\frac{W_{ch}(D_{jet,1}/2) - \frac{\pi(D_{jet,1}/2)^2}{4}}{p_h D_{jet,1}} \right)^b + C_3 Re_{jet,1}^c \left\{ \frac{\pi(D_{jet,1}/2)}{W_{ch} H_{ch}} \left[\frac{L_{jet,1}/2}{D_{jet,1}} - \frac{W_{ch}}{p_h} \left(\frac{1}{2} + \frac{\pi(D_{jet,1}/2)^2}{4 W_{ch} D_{jet,1}} \right) \right] \right\}^c. \quad (14)$$

The rest of the single-phase correlation can be obtained by simply setting $U_{jet,1} = U_{jet,1}/2$ and $D_{jet,1} = D_{jet,1}/2$ to the third term in Eqs. (12) and (13).

As indicated in [16] and recommended earlier by Wadsworth and Mudawar [9], the impingement term should be fitted with the exponent $a = 0.5$. The remaining empirical constants are obtained with a least-squares' fit to the single-phase heat transfer data. The following correlation was obtained for the micro-channel/micro-circular-jet-impingement module with equal-jet-size [16],

$$\frac{\overline{Nu}_L}{Pr_f^{0.4}} = \sum_{i=1}^{N_{jet}} \left\{ 63.41 Re_{jet,i}^{0.5} \left(\frac{D_{jet,i}}{p_h} \right) + 0.183 Re_{jet,i}^{0.199} \left(\frac{W_{ch} D_{jet,i} - \frac{\pi D_{jet,i}^2}{4}}{p_h D_{jet,i}} \right)^{0.199} + 0.197 Re_{jet,i}^{0.654} \left[\sum_{j=1}^i \left\{ \frac{\left(\frac{U_{jet,i}}{U_{jet,i}} \right) \frac{\pi D_{jet,i}^2}{4}}{W_{ch} H_{ch}} \right\} \times \left[\frac{L_{jet,i}}{D_{jet,i}} - \frac{W_{ch}}{p_h} \left(1 + \frac{\pi D_{jet,i}^2}{4 W_{ch} D_{jet,i}} \right) \right] \right]^{0.654} \right\}, \quad (15)$$

which can also be expressed as

$$\frac{\overline{Nu}_L}{Pr_f^{0.4}} = \sum_{i=1}^{N_{jet}} \sum_{j=1}^i \left\{ 63.41 Re_{jet,i}^{0.5} \left(\frac{D_{jet,i}}{p_h} \right) \left(\frac{1}{i} \right) + 0.183 Re_{jet,i}^{0.199} \left(\frac{W_{ch} D_{jet,i} - \frac{\pi D_{jet,i}^2}{4}}{p_h D_{jet,i}} \right)^{0.199} \left(\frac{1}{i} \right) + 0.197 Re_{jet,i}^{0.654} \left[\frac{\left(\frac{U_{jet,i}}{U_{jet,i}} \right) \frac{\pi D_{jet,i}^2}{4}}{W_{ch} H_{ch}} \left[\frac{L_{jet,i}}{D_{jet,i}} - \frac{W_{ch}}{p_h} \left(1 + \frac{\pi D_{jet,i}^2}{4 W_{ch} D_{jet,i}} \right) \right] \right]^{0.654} \right\}. \quad (16)$$

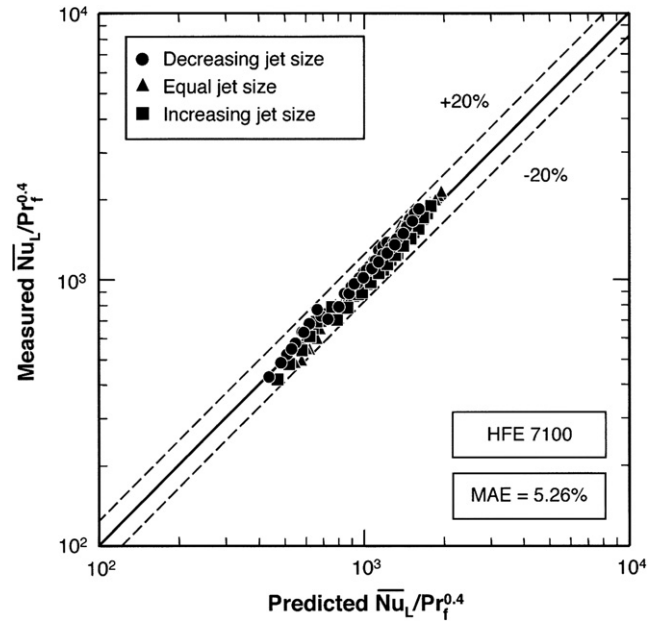


Fig. 6. Comparison of predictions of single-phase heat transfer correlation and experimental data.

Fig. 6 shows Eqs. (15) or (16) fit the single-phase data for all three micro-jet patterns with a mean absolute error (MAE) of 5.26%, with all data points falling within a $\pm 20\%$ error band. This is proof of the universal validity of this correlation.

5. Numerical predictions of the effects of micro-jet pattern

5.1. Validation of numerical predictions

Fig. 7 compares numerical predictions of the temperature distribution along the thermocouple line in the copper block with the thermocouple measurements for the three jet

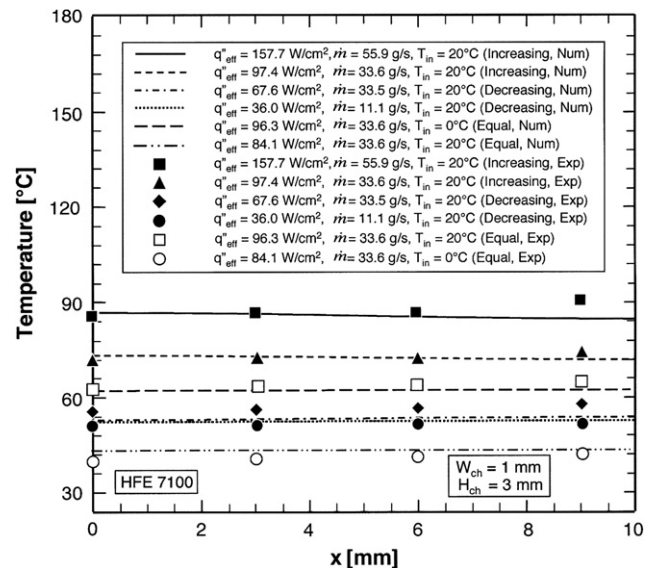


Fig. 7. Comparison of numerical predictions of temperatures along thermocouple line and measured temperatures.

patterns. The numerical scheme appears equally effective at predicting the temperature variations for the different jet patterns corresponding to different heat fluxes and flow rates. The agreement between the measured and predicted temperatures demonstrates the effectiveness of the present numerical scheme using the standard $k-\epsilon$ model and the relations used to determine the extent of the laminar zone.

5.2. Predicted trends of cooling performance

Figs. 8–10 show flow streamlines and channel bottom wall temperature distribution for one-fourth the unit cell illustrated in Fig. 3. Results for the three jet patterns are provided for low, medium, high flow rates in Figs. 8–10, respectively.

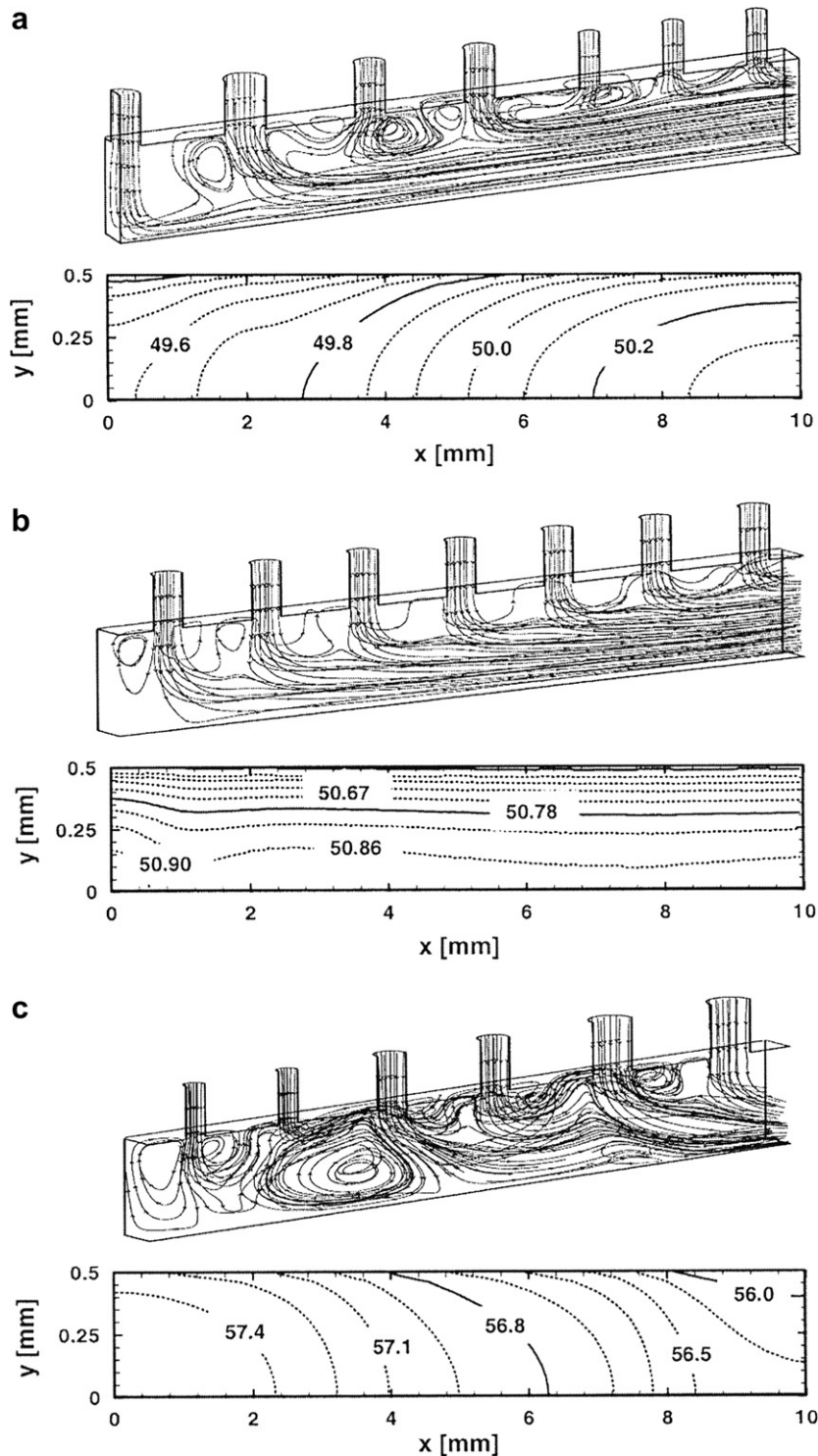


Fig. 8. Streamlines and wall temperature plots at $q''_{eff} = 36.0 \text{ W/cm}^2$, $\dot{m} = 11.1 \text{ g/s}$ for (a) decreasing-jet-size, (b) equal-jet-size, and (c) increasing-jet-size.

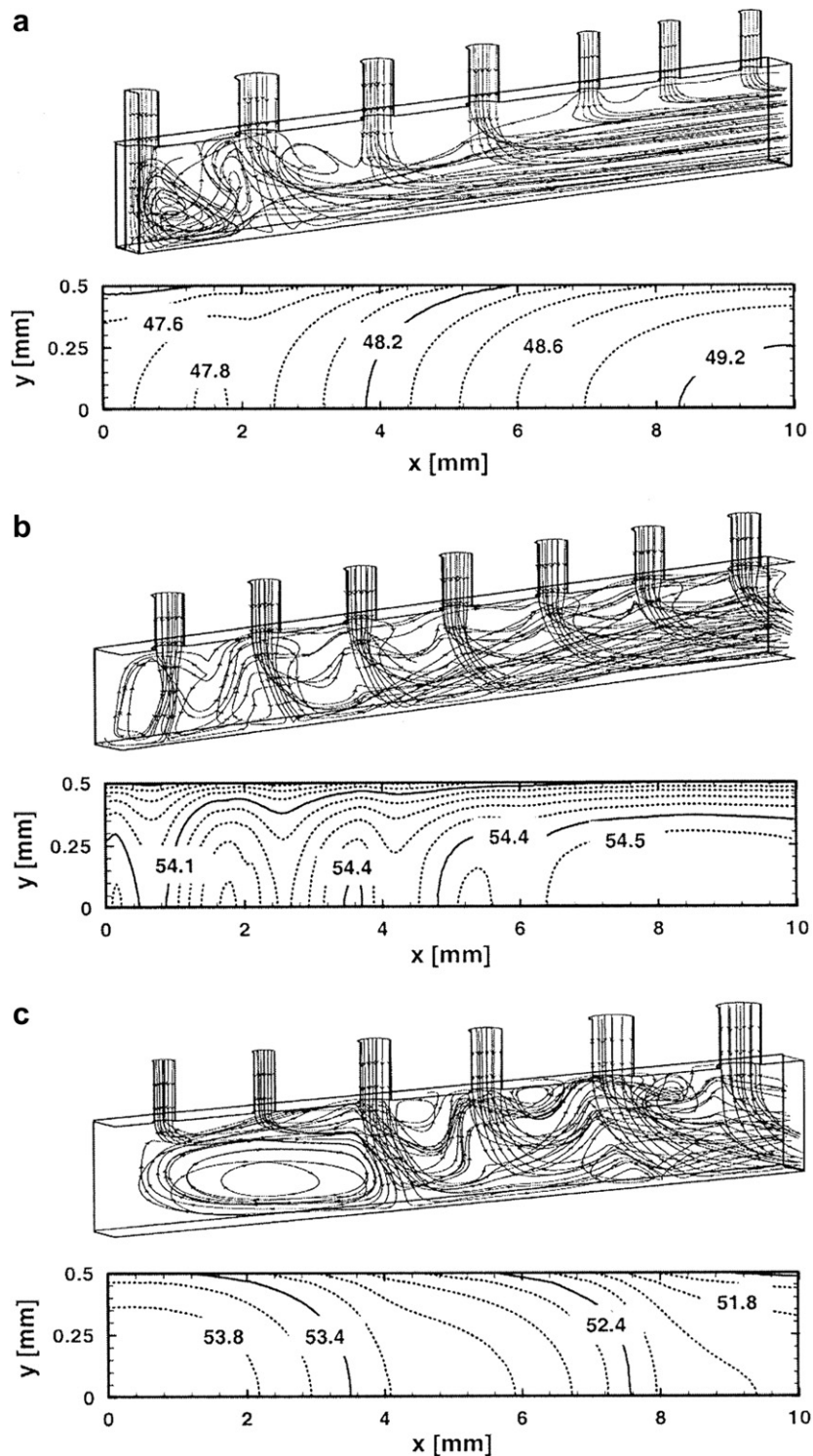


Fig. 9. Streamline and wall temperature plots at $q''_{\text{eff}} = 67.6 \text{ W/cm}^2$, $\dot{m} = 33.6 \text{ g/s}$ for (a) decreasing-jet-size, (b) equal-jet-size, and (c) increasing-jet-size.

For the decreasing-jet-size pattern with a low flow rate, Fig. 8a shows the large jets near the center of the channel are easily able to reach the channel bottom wall, yielding lowest temperatures near the center of the channel. The spent fluid from the first jet and second jet makes it difficult for the downstream jets to reach the bottom wall. However, the heat transfer coefficient increases with increasing

flow rate along the flow direction. The decreasing-jet-size pattern appears to effectively utilize both the jet flow and the channel flow to achieve excellent bottom wall temperature uniformity. Fig. 8b shows that heat transfer for the equal-jet-size pattern is dominated more by channel flow than by jet-impingement. Since the flow rate increases along the flow direction, the lowest temperature is

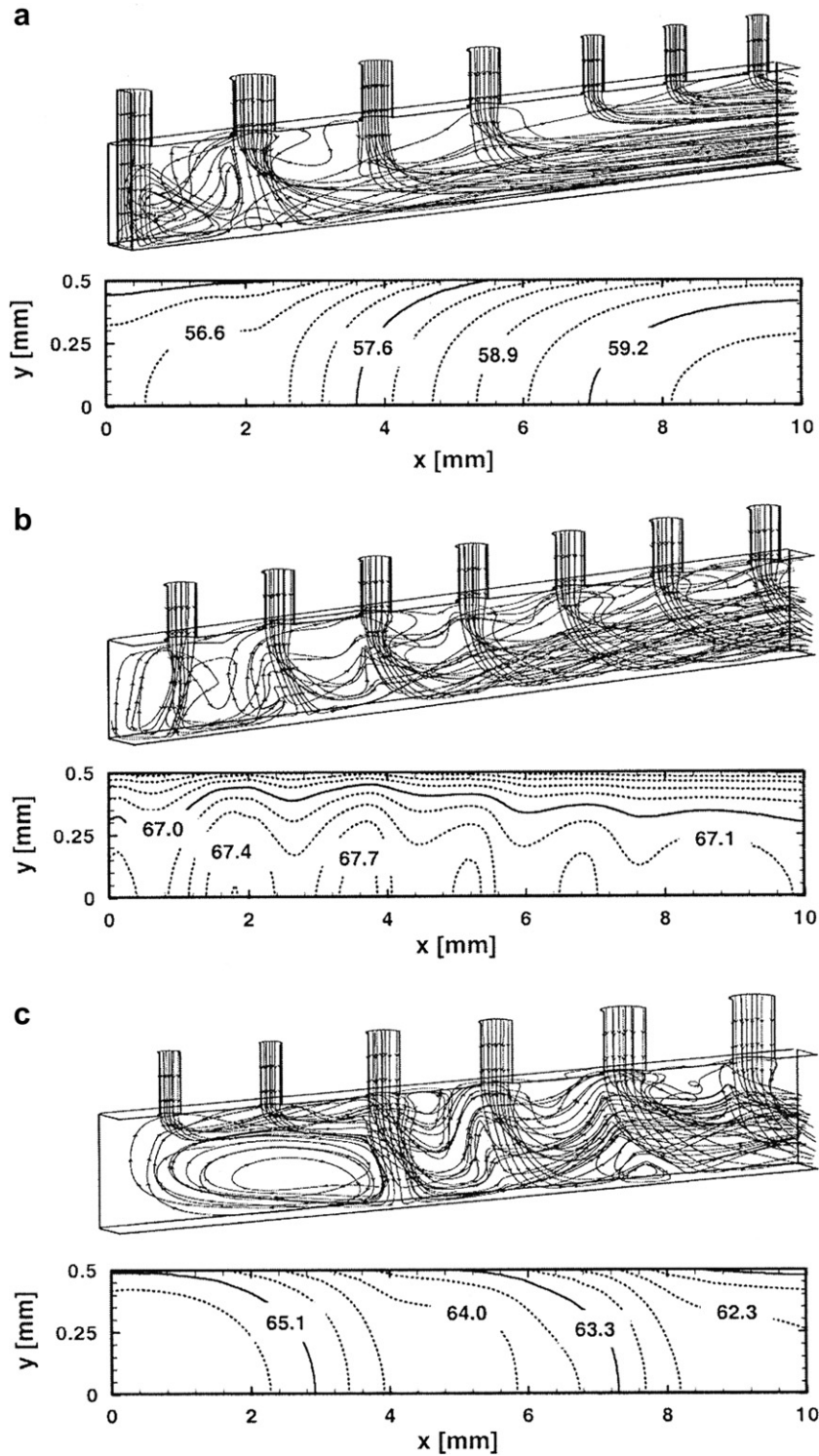


Fig. 10. Streamlines and wall temperature plots at $q''_{\text{eff}} = 121.5 \text{ W/cm}^2$, $\dot{m} = 55.9 \text{ g/s}$ for (a) decreasing-jet-size, (b) equal-jet-size, and (c) increasing-jet-size.

encountered near the channel outlet. For the increasing-jet-size pattern, Fig. 8c shows the flow is complicated by interactions between neighboring jets. Large jets near the channel outlet create appreciable blockage to coolant flow from the upstream small- and medium-sized jets. Overall, the increasing-jet-size pattern provides the poorest cooling per-

formance of the three jet patterns, evidenced by the highest wall temperatures and largest wall temperature gradients.

Figs. 9 and 10 show, for medium and high flow rates, respectively, similar cooling trends for each jet patterns. One obvious difference from the low flow rate case is a greater influence of jet-impingement compared to micro-

channel flow for all jet patterns. Strong impingement of the largest jets reduces surface temperature for the decreasing-jet-size pattern, Figs. 9a and 10a, and the increasing-jet-size pattern, Figs. 9c and 10c, compared to the equal-jet-size pattern, Figs. 9b and 10b. Because of the increasing flow rate along the flow direction, fairly uniform temperature is achieved with the decreasing-jet-size pattern as shown in Figs. 9a and 10a. Excellent surface temperature uniformity is achieved with the equal-jet-size pattern at medium and high flow rates as shown in Figs. 9b and 10b. For the increasing-jet-size pattern, the increasing flow rate escalates the aforementioned blockage effect, causing appreciable recirculation in the flow from the upstream small jets as shown in Figs. 9c and 10c. Despite the ability to achieve relatively low overall wall temperatures, the flow blockage induces large wall temperature gradients for the increasing-jet-size pattern.

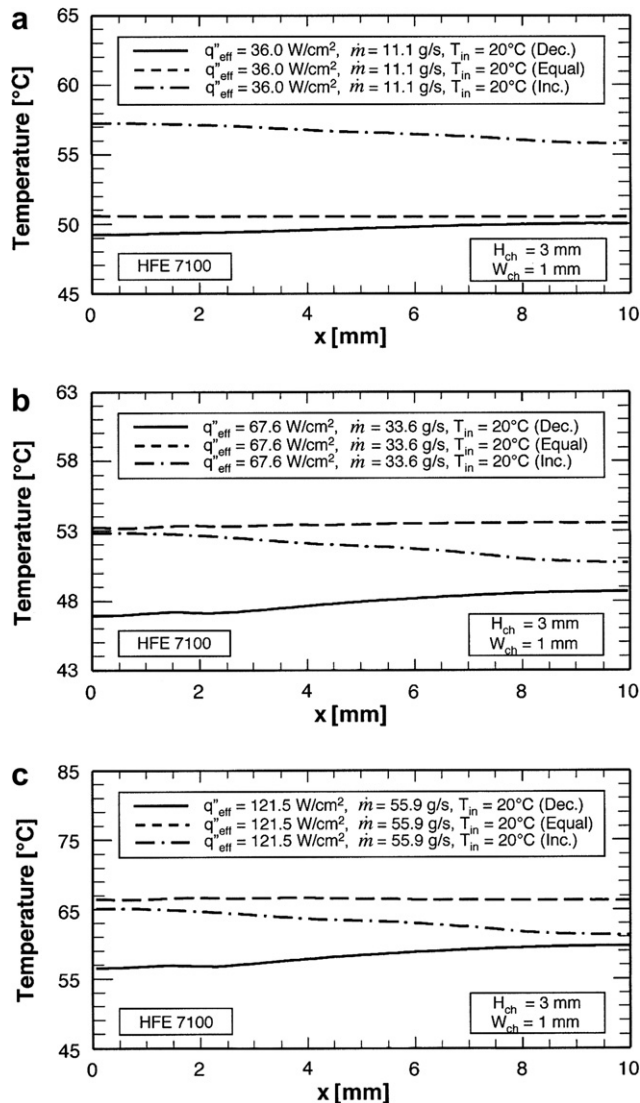


Fig. 11. Variation of wall Wadsworth and Mudawar [x]. temperature along micro-channel for (a) $q''_{\text{eff}} = 36.0 \text{ W/cm}^2$, $\dot{m} = 11.1 \text{ g/s}$, (b) $q''_{\text{eff}} = 67.6 \text{ W/cm}^2$, $\dot{m} = 33.6 \text{ g/s}$, and (c) $q''_{\text{eff}} = 121.5 \text{ W/cm}^2$, $\dot{m} = 55.9 \text{ g/s}$.

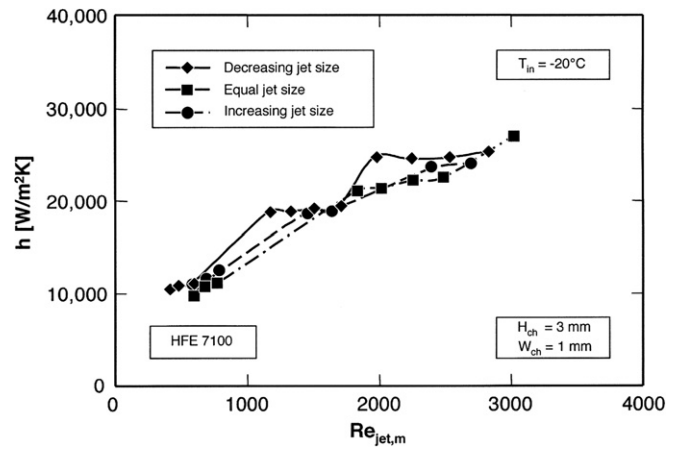


Fig. 12. Variation of heat transfer coefficient with mean jet Reynolds number for different jet patterns.

Fig. 11 shows the effects of flow rate on temperature distribution along the centerline of the channel's bottom wall. For the three jet patterns, increasing flow rate decreases the bottom wall temperature at the expense of a higher temperature gradient. The medium and high flow rate cases manifest the strong impingement effects of the large jets in the form of low upstream temperatures for the decreasing-jet-size pattern, Fig. 11a, and low downstream temperatures for the increasing-jet-size pattern, Fig. 11c. Fig. 11 shows, for all flow rates, the highest single-phase heat transfer coefficients (i.e., lowest wall temperatures) are achieved with the decreasing-jet-size pattern. However, the greatest temperature uniformity is realized with the equal-jet-size pattern. These trends point to important practical trends in cooling system design. The increasing-jet-size pattern is preferred for high-heat-flux removal, while the equal-jet-size pattern is preferred for devices demanding greater temperature uniformity.

The flow rate trends depicted in Fig. 11 are further substantiated in Fig. 12, which shows the heat transfer coefficient data plotted against $Re_{\text{jet},m}$, the jet Reynolds number based on mean velocity of all jets in a micro-jet plate. Clearly evident in Fig. 12 is the advantageous effect of increasing $Re_{\text{jet},m}$ for all jet patterns, as well as the superior heat transfer performance of the decreasing-jet-size pattern.

6. Conclusions

This study examined a hybrid thermal management scheme that combines the cooling benefits of micro-channel flow and jet-impingement. Indirect refrigeration cooling is used to achieve low coolant temperatures in order to decrease wall temperature during high-flux heat dissipation. Three micro-jet patterns are examined, decreasing-jet-size, equal-jet-size and increasing-jet-size. The performance of each pattern is examined experimentally and numerically using HFE 7100 as working fluid. Key findings from the study are as follows:

1. A single-phase correlation is developed using a superpositioning technique that assigns different heat transfer coefficient values to different regions of the micro-channel based on the dominant heat transfer mechanism for each region. A single correlation is found equally effective at fitting experimental data for all three micro-jet patterns.
2. Excellent agreement between numerical predictions and temperature measurements proves the standard $k-\epsilon$ model and the criteria adopted to determine the extent of the laminar zone are very effective at predicting the heat transfer performance of the hybrid cooling scheme regardless of micro-jet pattern.
3. The three hybrid module configurations involve complex interactions of impinging jets with micro-channel flow. Increasing the flow rate (and therefore jet speed) strengthens the contribution of jet impingement to the overall cooling performance, resulting in lower overall bottom wall temperatures. However, this advantage is realized at the expense of greater wall temperature gradients.
4. The highest convective heat transfer coefficients and lowest bottom wall temperatures are achieved with the decreasing-jet-size pattern, rendering this pattern most suitable for applications demanding high-heat-flux removal. The equal-jet-size pattern provides the smallest gradients in bottom wall temperature; this pattern is therefore better suited to devices demanding temperature uniformity. The increasing-jet-size pattern produces complex flow patterns and greater wall temperature gradients, which are caused by blockage of the spent fluid by larger jets near the channel outlets.

Acknowledgement

The authors are grateful for the financial support of the Office of Naval Research (ONR).

References

- [1] I. Mudawar, Assessment of high-heat-flux thermal management schemes, *IEEE Trans. Compon. Pack. Tech.* 24 (2001) 122–141.
- [2] D.B. Tuckerman, R.F.W. Pease, High-performance heat sinking for VLSI, *IEEE Electron Device Lett.* EDL-2 (1981) 126–129.
- [3] M.B. Bowers, I. Mudawar, High flux boiling in low flow rate, low pressure drop mini-channel and micro-channel heat sinks, *Int. J. Heat Mass Transfer* 37 (1994) 321–332.
- [4] W. Qu, I. Mudawar, Experimental and numerical study of pressure drop and heat transfer in a single-phase micro-channel heat sink, *Int. J. Heat Mass Transfer* 45 (2002) 2549–2565.
- [5] S.J. Kim, D. Kim, Forced convection in microstructures for electronic equipment cooling, *J. Heat Transfer* 121 (1999) 639–645.
- [6] A.G. Fedorov, R. Viskanta, Three-dimensional conjugate heat transfer in the microchannel heat sink for electronic packaging, *Int. J. Heat Mass Transfer* 43 (2000) 399–415.
- [7] H. Martin, Heat and mass transfer between impinging gas jets and solid surfaces, *Adv. Heat Transfer* 13 (1977) 1–60.
- [8] L.M. Jiji, Z. Dagan, Experimental investigation of single-phase multi-jet impingement cooling of array of microelectronic heat sources, in: *Proceedings of the International Symposium on Cooling Technology for Electronic Equipment*, Honolulu, HI, 1987, pp. 265–283.
- [9] D.C. Wadsworth, I. Mudawar, Cooling of a multichip electronic module by means of confined two-dimensional jets of dielectric liquid, *J. Heat Transfer* 112 (1990) 891–898.
- [10] T.J. Craft, L.J.W. Graham, B.E. Launder, Impinging jet studies for turbulence model assessment – II. An examination of the performance of four turbulence models, *Int. J. Heat Mass Transfer* 36 (1993) 2685–2697.
- [11] T.H. Park, H.G. Choi, J.Y. Yoo, S.J. Kim, Streamline upwind numerical simulation of two-dimensional confined impinging slot jets, *Int. J. Heat Mass Transfer* 46 (2003) 251–262.
- [12] E. Baydar, Y. Ozmen, An experimental and numerical investigation on a confined impinging air jet at high Reynolds numbers, *App. Thermal Eng.* 25 (2005) 409–421.
- [13] W.A. Little, Low temperature electronics workshop: recent advances in low cost cryogenic coolers for electronics, in: *Proceedings of 16th IEEE Semi-Therm Symposium*, San Jose, CA, 2000, pp. 110–111.
- [14] A. Naeemi, J.D. Meindl, An upper limit for aggregate I/O interconnect bandwidth of GSI chips constrained by power dissipation, in: *Proceedings of IEEE International Interconnect Technology Conference*, San Francisco, CA, 2004, pp. 157–159.
- [15] R.R. Schmidt, B.D. Notohardjono, High-end server low-temperature cooling, *IBM J. Res. Dev.* 49 (2002) 739–751.
- [16] M.K. Sung, I. Mudawar, Single-phase hybrid micro-channel/micro-jet-impingement cooling, *Int. J. Heat Mass Transfer* 51 (2008) 4342–4352.
- [17] M.K. Sung, I. Mudawar, Single-phase and two-phase heat transfer characteristics of low temperature hybrid micro-channel/micro-jet-impingement cooling module, *Int. J. Heat Mass Transfer* 51 (2008) 3882–3895.
- [18] Fluent 6.2.16. User's Guide, Fluent Inc., Lebanon, NH, 2005.
- [19] Gambit 2.2.30. User's Guide, Fluent Inc., Lebanon, NH, 2006.
- [20] B.E. Launder, D.B. Spalding, The numerical computation of turbulent flows, *Comput. Meth. Appl. Mech. Eng.* 3 (1974) 269–289.
- [21] F.P. Incropera, *Liquid Cooling of Electronic Devices by Single-phase Convection*, Wiley, New York, NY, 1999.